Clogging of a Rectangular Slit by a Spherical Soft Particle

Charles Paul Moore, Julien Husson, Arezki Boudaoud, Gabriel Amselem, Charles Baroud

Clogging of a Rectangular Slit by a Spherical Soft Particle

Charles Paul Moore,[1,2] Julien Husson,[2] Arezki Boudaoud,[2] Gabriel Amselem,[2] and Charles N. Baroud[1,2]
[1]Institut Pasteur, Université Paris Cité, Physical microfluidics and Bioengineering, 25-28 Rue du Dr Roux, 75015 Paris, France
[2]Laboratoire d'Hydrodynamique (LadHyX), CNRS, Ecole Polytechnique, Institut Polytechnique de Paris, 91120 Palaiseau, France

(Received 27 June 2022; accepted 3 January 2023; published 7 February 2023)

The capture of a soft spherical particle in a rectangular slit leads to a nonmonotonic pressure-flow rate relation at low Reynolds number. Simulations reveal that the flow induced deformations of the trapped particle focus the streamlines and pressure drop to a small region. This increases the resistance to flow by several orders of magnitude as the driving pressure is increased. As a result, two regimes are observed in experiments and simulations: a flow-dominated regime for small particle deformations, where flow rate increases with pressure, and an elastic-dominated regime in which solid deformations block the flow.

DOI: 10.1103/PhysRevLett.130.064001

Solid deformations can have a major influence on fluid flow in the regime of strong fluid-structure coupling. A wide range of complex behaviors, including oscillations that lead to catastrophic failures or blockages, can be observed when the inertial effects of the fluid and solid couple together [1]. Recently increased attention has been paid to the effect of a low Reynolds number flow on an elastic fiber [2], with particular focus on the transport [3] and deformation [4] of slender elastic fibers by the flow [5].

Two-way flow-structure coupling has been studied in the case of deformable tubes, in which elastic deformations of the tube walls led to strong modifications of the fluid flow. Wall elasticity effects were shown to stabilize the flow distribution into a bifurcation [6] and to suppress the emergence of viscous fingering in a Hele-Shaw cell [7]. More extreme cases emerged in the case of air-liquid flows within flexible tubes, where surface tension led to a complete airway closure [8]. These effects of wall elasticity of the fluid flow have been used to explain sap flow in green plants [9] or to create soft valves for technological applications [10–12].

A different class of problems for which the two-way coupling can lead to extreme modifications of the flow consists of the case of a soft particle being pushed into an orifice. This problem is encountered in many microfluidic applications, such as during the flow and encapsulation of hydrogels [13,14] or for the characterization of cells and other soft materials [15–20]. It is also closely related to clogging or sieving particles [21–28]. In many of these cases a spherical particle is pushed into a rectangular slit, which allows for a leakage flow around the particle [15,17,19,29]. But in spite of the interest for applications, the physics that determines the equilibrium between leaky flow and particle deformation has not been explored. Here we describe this relationship and explain the low and high deformation regimes that are encountered.

The experimental setup consists of a polydimethylsiloxane (PDMS) microfluidic device (Young's modulus $E_{\mathrm{PDMS}} = 1$–10 MPa) with two parallel channels: a thrupass line with a narrow slit, to trap microgel beads, and a bypass of width $y_{\max}$, which provides a known hydraulic resistance (see Fig. 1). The flow rate Q is imposed at the inlet and streamlines of the flow in the device are reconstructed [30], see Fig. 1(a). The flow rate Q_{thru} in the thrupass channel is determined by measuring the position y of the separatrix streamline, taken one channel width upstream of the junction [see inset in Fig. 1(b)]. This separatrix divides the fluid going to the thrupass and the bypass channels according to $Q_{\mathrm{thru}} = Q \int_0^y U(y)\,dy / \int_0^{y_{\max}} U(y)\,dy$, where $U(y)$ is the empirically calculated flow speed in a rectangular channel of height h and width $y_{\max}$ [31].

In the absence of a gel bead, increasing the flow rate Q at the inlet led to an increase of the flow rate Q_{thru}, with the ratio between Q_{thru} and Q being given by the ratio of the hydrodynamic resistances between the thrupass and bypass channels. When a gel bead was trapped by the narrow slit, increasing the flow rate Q at the inlet led to a nonmonotonic behavior of the flow rate Q_{thru} through the thrupass channel. At first, increasing Q led to an increase in Q_{thru}, until a maximum value of Q_{thru} was reached; increasing Q beyond a critical value then led to a decrease in the flow rate Q_{thru}, see Fig. 1(b). At high enough values of Q, the gel bead plugged the thrupass channel entirely and all the flow was redirected to the bypass channel. This nonmonotonic relationship between Q_{thru} and Q reveals a strong nonlinear hydrodynamic resistance added by the gel bead.

Experiments were repeated for poly(ethylene glycol) (PEG) beads of diameters $d = 80$–145 μm. The beads were

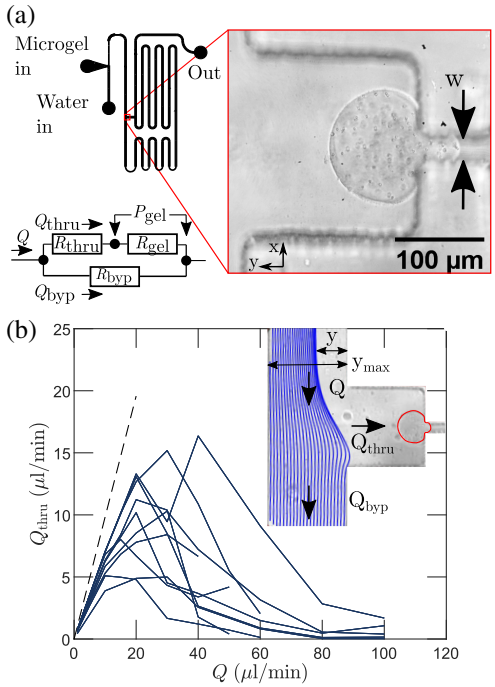

FIG. 1. (a) Sketch of the microfluidic device. The flow rate is imposed at the inlet and divides into a thrupass channel and a bypass channel. The micrograph shows a gel bead trapped in a slit of width $w = 25$ μm. A resistance diagram of the microfluidic channel is included. (b) The flow rate Q_{thru} past the microgel increases to a maximum and then decreases to zero as the inlet flow rate Q is increased. Each line represents a different trapped microgel. Equivalent Young's modulus $E^* = 15 \pm 9$ kPa. Gel diameter: $d = 83 \pm 3$ μm. Slit width: $w = 25 \pm 5$ μm. Channel height: $h = 85$ μm. Inset: reconstructed streamlines showing the flow division between the thrupass and bypass channels. The value of y/y_{max} provides a measure of the flow rates Q_{thru} and Q_{byp}.The black dashed line represents an empty trap.

made using droplet flow lithography by adding PEG-diacrylate (PEG-DA) to a PEG solution and photopolymerizing it in a first microfluidic device [32]. The beads were stored off-chip until they were reinjected into the current device. The microgel stiffness was controlled by modulating the ratio of PEG to PEG-DA. The values of the equivalent Young's moduli were obtained using a micro-indentation technique [33] and spanned 2 orders of magnitude: $E^\star = 112$ Pa to 15 kPa, where $E^\star = E/(1-\nu^2)$, E is the conventional Young's modulus and ν is the Poisson ratio. Three different microfluidic traps were used, ranging within $w = 15$–55 μm, and microchannel heights h chosen to approximately match microgel diameters: $h = d \pm 10\%$. Channel corner radii, r_c, varied with manufacturing and were measured directly on the microscopy images.

The Reynolds number $\mathrm{Re} = [2Q/\eta(w+h)]$, where η is the kinematic fluid viscosity, was in the range $0.01 < \mathrm{Re} < 6$ in the inlet channel. Its value around the hydrogel was significantly lower, however, given the lower velocities and smaller length scale. In this regime the pressure ΔP across a channel is proportional to the flow rate Q in the channel and the hydrodynamic resistance R of the channel: $\Delta P = QR$ [34]. Calling R_{thru} and R_{byp} the known hydrodynamic resistances of the thrupass and bypass channels, respectively, in the absence of gel, and R_{gel} the added hydrodynamic resistance of the gel, we therefore have $(Q_{byp}/Q_{thru}) = [(R_{thru} + R_{gel})/R_{byp}]$. This relation provides a way to compute the resistance R_{gel} added by the gel, as well as the pressure drop across the gel $P_{gel} = R_{gel}Q_{thru}$ [see Fig. 1(a)].

The value of R_{gel} increased dramatically with flow rate, spanning nearly 6 orders of magnitude when the flow rates covered 2 orders of magnitude [see Fig. 2(a)]. The rate of this increase depended on the gel elasticity: stiffer gels ($E^\star \approx 10^4$ Pa) led to a slower increase in resistance than softer gels ($E^\star \approx 10^2$ Pa). The increase in resistance was associated with a displacement of the microgel as it deformed and penetrated into the slit. This displacement was quantified by measuring the distance l traveled by the back of the gel, i.e., upstream of the slit, with respect to its position in the absence of flow [see inset in Fig. 2(b)]. The value of l increased with the pressure drop across the gel P_{gel}, see Fig. 2(b). For a given pressure P_{gel} across the gel bead, the softer gels penetrated more into the slit, and even more so when the gap width was larger, see Fig. 2(b).

To understand how the flow forced the hydrogel to deform, plug the slit, and increase the hydrodynamic resistance, simulations of a soft particle deforming into a slit were performed on a quarter-setup using the software ABAQUS. The solid deformations were modeled by simulating an initially spherical gel bead, $d = 80$ μm, $r_c = w = 15$ μm, $E = 10$ kPa, $\nu = 0.35$ [35], that was subjected to a negative pressure, $0 \le P_{sim} \le 4.8$ kPa, inside the slit. The resulting deformed gel geometry [Fig. 3(a)] was exported to the software COMSOL Multiphysics and the

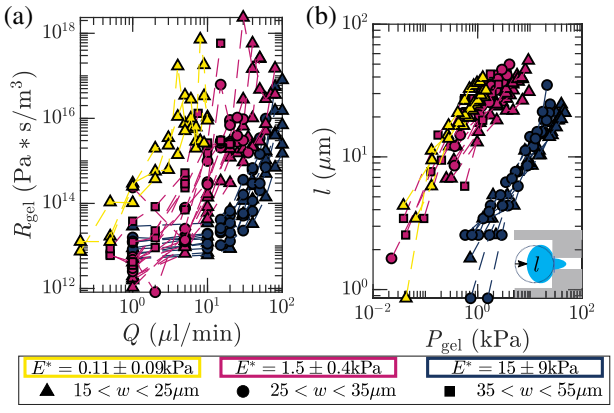

FIG. 2. (a) Hydrodynamic resistance due to the gel R_{gel}, as a function of the imposed flow rate Q. Note that the resistance increases faster for softer gels than stiffer gels. (b) Microgel displacement as a function of the applied pressure. Each curve represents data collected on a single microgel.

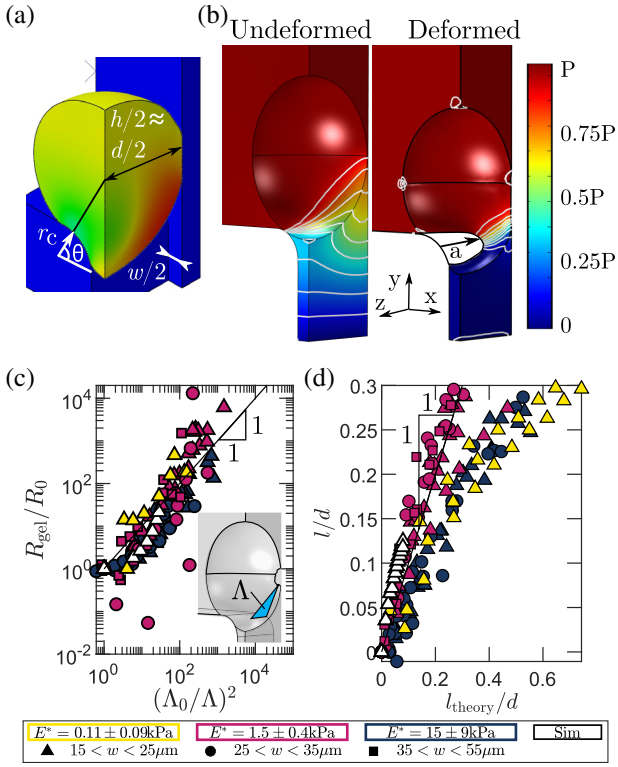

FIG. 3. (a) A quarter section of the deformed microgel and trap for an applied pressure $P_{gel} = 4$ kPa. Color represents relative nodal displacement in the microgel. (b) Simulation of the flow around an undeformed gel (left), and a gel deformed under a simulated pressure of $P_{gel} = 4$ kPa (right). Color indicates the pressure normalized by the inlet pressure P. Isobars are shown in white. Note how the deformed microgel focuses the pressure drop into a narrow area. x and y directions represent the imaging plane. (c) The measured gel hydrodynamic resistance R_{gel} as a function of the area Λ of the triangle through which the flow must pass (see inset). R_{gel} and Λ are, respectively, normalized by the resistance to flow R_0 and the area Λ_0 in the absence of gel deformation. (d) A comparison of the measured normalized deformation of the microgel l/d with its predicted deformation based on solid contact, l_{theory}/d, where l represents the penetration distance of the microgel and d the undeformed microgel diameter. The graphs include experimental (color) and simulation results (white). Data are limited to the range $l/d < 0.3$ to remain within the valid range of Eq. (3), see Supplemental Material for details.

flow field in the channel containing the deformed gel was simulated, providing the pressure distribution in the fluid everywhere in the device. The uncoupled solid and fluid simulations were then iterated once by updating the gel shape and then the pressure field.

In the absence of deformation, the pressure drop in the channel occurred both around the spherical gel particle and in the slit, as shown by the isobars in the fluid simulations of Fig. 3(b) (left panel). When the gel deformed however, the pressure drop was focused over a short distance upstream of the slit, corresponding to the region where the flow was focused through a narrow gap of cross-sectional area Λ, see Fig. 3(b) right panel. This concentration of the pressure drop indicates that the resistance to flow was due not to the finger of gel elongating into the slit but rather to the bulblike part of the gel that obstructed the fluid flow upstream of it.

The physical reason behind the focusing of the pressure drop can be understood by considering the dependence of R_{gel} on Λ. This parameter can be related to other geometric parameters as [see Supplemental Material [36] and inset of Fig. 3(c)]

$$\Lambda \approx \left(\frac{d}{4} - \frac{a}{2}\right)\sqrt{\left(\frac{d}{2} - l - \frac{a}{2}\right)^2 + \left[\frac{w}{2} + r_c\left(1 - \frac{\sqrt{2}}{2}\right)\right]^2}, \tag{1}$$

where d is the bead diameter, w is the width of the slit, r_c is the radius of curvature of the corner of the slit [see Fig. 3(a)], and a is the extent of the contact area between the gel and the corner of the slit [see Fig. 3(b), right panel].

Because a is in a direction perpendicular to the imaging plane, it is inferred by considering the contact mechanics problem of a spherical elastic bead, of diameter d and elastic modulus $E^\star$, being pressed with a pressure P_{gel} on top of two cylinders of equal radius r_c and spaced by w [44]. The displacement of the gel l_{theory} due to this forcing was found to relate to the major axis a of the ellipsoidal contact between the microgel and the trap, modulated by a combination of the geometrical parameters of the problem (see Supplemental Material for full explanation):

$$l_{theory} = \frac{2a^2}{d\sin\theta}\mathcal{F}_1\left(\frac{r_c}{d}\right), \tag{2}$$

where $\mathcal{F}_1(r_c/d)$ is a function that describes the shape of contact (see Supplemental Material) and θ is the angle created between the microgel, the corner, and the slit [see Fig. 3(a)]. Equation (1) was therefore used to obtain the area Λ using direct measurements of d, w, r_c, and l, while a was estimated using Eq. (2) for each imposed flow rate.

Given the above geometric measurements it is now possible to determine the scaling of R_{gel} with the interstitial space Λ. Calling R_0 and Λ_0 the values of the parameters in the absence of gel deformation, i.e., at the lowest flow rate tested, we plot R_{gel}/R_0 as a function of $(\Lambda_0/\Lambda)^2$ in Fig. 3(c).

The plot shows an excellent collapse for all experimental and numerical results and indicates that R_{gel} scales as Λ^{-2}. This relationship recalls the scaling for Hagen-Poiseuille flow, where $R_{gel} \sim \Lambda^{-2}$, if the 3D variations in geometry are ignored and if we focus only on the point of maximum constriction. The collapse of the measurements of R_{gel} on a single master curve shows that the resistance to flow is indeed due to the deformation of the soft solid upstream of

the slit which in turn determines the size of the gap that the flow must go through. Moreover, the rapid increase of R_{gel} makes it the dominant source of pressure drop compared with the other sections in the rest of the microchannel.

In turn the added resistance due to flow focusing couples back to modify the shape of the microgel. This determines the values of l and a, which are related together by Eq. (2). Contact mechanics modeling shows that a depends on the ratio $P_{\mathrm{gel}}/E^{\star}$ and a combination of the geometric parameters, which yields an implicit relationship between mechanical and geometric effects:

$$\left(\frac{a}{d}\right)^3 = \frac{3P_{\mathrm{gel}}}{4\pi E^{\star}}\mathcal{F}_2\left(\frac{r_c}{d}\right) \times \left[\frac{aw + \frac{2}{3}\left(\frac{d}{2} - a\right)[w + r_c(1-\cos\theta)]}{d^2\sin\theta}\right], \quad (3)$$

where $\mathcal{F}_2(r_c/d)$ is another function of the shape of contact with the corner (see Supplemental Material).

The expected theoretical value of the rescaled gel elongation l_{theory}/d was calculated from Eqs. (2) and (3) and compared to the experimentally and numerically computed values of elongation, as shown in Fig. 3(d). Again the theory collapses the data onto a master curve, particularly for small deformations for which contact mechanics are expected to apply.

It is now possible to quantitatively understand the relationship between the pressure P_{gel} on the trapped soft bead and the flow Q_{thru} it lets pass through. Combining Eqs. (1)–(3), we find the following relationship between the normalized flow rate through the slit $\mathcal{Q} = Q_{\mathrm{thru}}R_0/E^{\star}$ and the normalized pressure drop $\mathcal{P} = P_{\mathrm{gel}}/E^{\star}$ across the gel:

$$\mathcal{Q} = C_1\mathcal{P}(1 - C_2\mathcal{P}^{\frac{1}{3}})^2[(1 - C_3\mathcal{P}^{\frac{2}{3}})^2 + C_4^2], \quad (4)$$

where the C_i are geometric parameters dependent upon w/d and r_c/d (see Supplemental Material).

The nonmonotonic dependence of $\mathcal{Q}$ on $\mathcal{P}$ can now be recovered by plotting the solutions of Eq. (4) for different geometric parameters, as shown in Fig. 4(a). For low values of $\mathcal{P}$ the pressure does not lead to significant deformation of the microgel, such that further increasing $\mathcal{P}$ leads to a nearly linear increase in $\mathcal{Q}$. When the pressure is increased beyond $\mathcal{P} = \mathcal{O}(1)$ the gel bead deformation increases the value of R_{gel} and leads to a decrease in the flow rate through the slit. The experiments agree semiquantitatively with the predictions above. Indeed nondimensionalizing the experimental data collapses flow rate and pressure values, which were originally spread over 3 orders of magnitude [Fig. 4(a) inset], to the same order of magnitude as the theoretical predictions [Fig. 4(a)].

Finally, Eq. (4) shows that the dimensionless flow rate $\mathcal{Q}$ depends only on the dimensionless pressure $\mathcal{P}$ and on the geometry of the slit, through the parameters C_1–C_4. For a given geometry it follows that $\mathcal{Q}$ traces a unique curve, of parameter $\mathcal{P}$, whose maximum value $\mathcal{Q}_{\mathrm{max}}$ only depends on the geometry of the slit. Therefore the maximum dimensional flow rate $Q_{\mathrm{max}} = \mathcal{Q}_{\mathrm{max}}E^{\star}/R_0$ scales linearly with the Young modulus of the gel $E^{\star}$: a soft gel deforms right away and plugs the channel at low pressures, while a stiff gel allows higher flow to go through. This linear increase is confirmed by comparing the largest measured flow rate with the prediction of Q_{max}, as shown in Fig. 4(b).

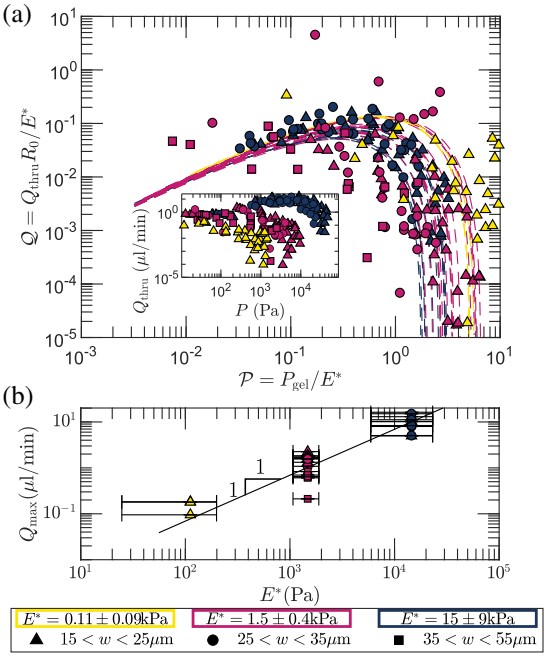

FIG. 4. (a) Comparison of flow rate through the obstructed thrupass channel, shown in points, with the predicted flow rate, shown as dashed lines. Normalized flow rates, $\mathcal{Q}$, are given as a function of the normalized pressure $\mathcal{P}$ for the full range of pressures tested experimentally. The inset shows the unscaled comparison of flow rates Q_{thru} with P_{gel}. (b) Maximum flow rate Q_{max} past the microgel as a function of the Young's modulus $E^{\star}$ of the trapped bead. Points: experimental data. Error bars represent 1 standard deviation. Line shown represents the linear best fit.

The results presented here provide a physical basis to understand the encapsulation of soft beads in droplets, which has emerged as an important microfluidic technology [45]. In a different operation regime, the strong nonlinear relationship between pressure and flow rate can lead to the design of microfluidic nonlinear flow elements, such as check valves or flow limiters. These devices play an important role in ensuring the robustness of fluidic circuits and protecting against surges. The analysis above shows that the maximum allowable flow rate scales linearly with $E^{\star}$, thus providing a simple design rule. Finally, the design of the slit presented here can also serve to measure the elastic modulus of soft materials, similarly to a micropipette aspiration device.

The authors acknowledge the microfabrication assistance of Caroline Frot at Ecole Polytechnique and the Biomaterials and Microfluidics platforms at Institut Pasteur. Useful discussions with Hiba Belkadi and Mahdi Daei Daei are also acknowledged.

[1] M. P. Païdoussis, S. J. Price, and E. De Langre, *Fluid-Structure Interactions: Cross-Flow-Induced Instabilities* (Cambridge University Press, Cambridge, England, 2010).
[2] C. Duprat and H. A. Stone, *Fluid-Structure Interactions in Low-Reynolds-Number Flows* (Royal Society of Chemistry, Cambridge, 2015).
[3] Y. Liu, B. Chakrabarti, D. Saintillan, A. Lindner, and O. Du Roure, Proc. Natl. Acad. Sci. U.S.A. **115**, 9438 (2018).
[4] C. Duprat, H. Berthet, J. S. Wexler, O. Du Roure, and A. Lindner, Lab Chip **15**, 244 (2015).
[5] O. Du Roure, A. Lindner, E. N. Nazockdast, and M. J. Shelley, Annu. Rev. Fluid Mech. **51**, 539 (2019).
[6] C. N. Baroud, S. Tsikata, and M. Heil, J. Fluid Mech. **546**, 285 (2006).
[7] D. Pihler-Puzović, R. Périllat, M. Russell, A. Juel, and M. Heil, J. Fluid Mech. **731**, 162 (2013).
[8] A. L. Hazel and M. Heil, Proc. R. Soc. A **461**, 1847 (2005).
[9] K. H. Jensen, K. Berg-Sørensen, H. Bruus, N. M. Holbrook, J. Liesche, A. Schulz, M. A. Zwieniecki, and T. Bohr, Rev. Mod. Phys. **88**, 035007 (2016).
[10] D. Kim and D. J. Beebe, Sens. Actuators B **136**, 426 (2007).
[11] J.-F. Louf, J. Knoblauch, and K. H. Jensen, Phys. Rev. Lett. **125**, 098101 (2020).
[12] E. Chappel, Appl. Sci. **10**, 8858 (2020).
[13] A. R. Abate, C.-H. Chen, J. J. Agresti, and D. A. Weitz, Lab Chip **9**, 2628 (2009).
[14] A. M. Klein, L. Mazutis, I. Akartuna, N. Tallapragada, A. Veres, V. Li, L. Peshkin, D. A. Weitz, and M. W. Kirschner, Cell **161**, 1187 (2015).
[15] Y. Luo, D. Chen, Y. Zhao, C. Wei, X. Zhao, W. Yue, R. Long, J. Wang, and J. Chen, Sens. Actuators B **202**, 1183 (2014).
[16] M. Elias, A. Dutoya, A. Laborde, A. Lecestre, C. Montis, L. Caselli, D. Berti, B. Lonetti, C. Roux, and P. Joseph, Micro Nano Eng. **8**, 100064 (2020).
[17] P. Preira, M.-P. Valignat, J. Bico, and O. Théodoly, Biomicrofluidics **7**, 024111 (2013).
[18] S. Tlili, F. Graner, and H. Delanoë-Ayari, Development **149**, 200774 (2022).
[19] Z. Zhang, J. Xu, and C. Drapaca, Microfluid. Nanofluid. **22**, 120 (2018).
[20] Y. Xu, H. Zhu, Y. Shen, A. P. M. Guttenplan, K. L. Saar, Y. Lu, D. Vigolo, L. S. Itzhaki, and T. P. J. Knowles, MRS Bull. **47**, 119 (2022).
[21] K. Harth, J. Wang, T. Börzsönyi, and R. Stannarius, Soft Matter **16**, 8013 (2020).
[22] E. Dressaire and A. Sauret, Soft Matter **13**, 37 (2017).
[23] G. C. Agbangla, P. Bacchin, and E. Climent, Soft Matter **10**, 6303 (2014).
[24] R. Tao, M. Wilson, and E. R. Weeks, Phys. Rev. E **104**, 044909 (2021).
[25] X. Hong, K. W. Desmond, D. Chen, and E. R. Weeks, Phys. Rev. E **105**, 014603 (2022).
[26] S. Alborzi, B. Clark, and S. M. Hashmi, Soft Matter **18**, 4127 (2022).
[27] Y. Yoon, S. Kim, J. Lee, J. Choi, R.-K. Kim, S.-J. Lee, O. Sul, and S.-B. Lee, Sci. Rep. **6**, 26531 (2016).
[28] A. Le Goff, B. Kaoui, G. Kurzawa, B. Haszon, and A.-V. Salsac, Soft Matter **13**, 7644 (2017).
[29] Z. S. Khan, N. Kamyabi, F. Hussain, and S. A. Vanapalli, Convergent Sci. Phys. Oncol. **3**, 024001 (2017).
[30] C. Guermonprez, S. Michelin, and C. N. Baroud, Biomicrofluidics **9**, 054119 (2015).
[31] S. A. Vanapalli, D. van den Ende, M. H. G. Duits, and F. Mugele, Appl. Phys. Lett. **90**, 114109 (2007).
[32] D. Dendukuri, K. Tsoi, T. A. Hatton, and P. S. Doyle, Langmuir **21**, 2113 (2005).
[33] L. Guillou, A. Babataheri, P.-H. Puech, A. I. Barakat, and J. Husson, Sci. Rep. **6**, 21529 (2016).
[34] H. Bruus, *Theoretical Microfluidics* (Oxford University Press, New York, 2007), Vol. 18.
[35] J. Cappello, V. d'Herbemont, A. Lindner, and O. du Roure, Micromachines (Basel) **11**, 318 (2020).
[36] See Supplemental Material at http://link.aps.org/supplemental/10.1103/PhysRevLett.130.064001 for a precise description of the methods, as well as a precise description of the geometric approximations used in the text, which includes Refs. [37–43].
[37] E. Verneuil, M. Cordero, F. Gallaire, and C. Baroud, Langmuir **25**, 5127 (2009).
[38] N. A. Mortensen, F. Okkels, and H. Bruus, Phys. Rev. E **71**, 057301 (2005).
[39] S. A. Vanapalli, A. G. Banpurkar, D. van den Ende, M. H. G. Duits, and F. Mugele, Lab Chip **9**, 982 (2009).
[40] D. Qin, Y. Xia, and G. M. Whitesides, Nat. Protocols **5**, 491 (2010).
[41] K. Izdihar, H. R. Abdul Razak, N. Supion, M. K. A. Karim, N. H. Osman, and M. Norkhairunnisa, Appl. Sci. **11**, 1172 (2021).
[42] I. D. Johnston, D. K. McCluskey, C. K. L. Tan, and M. C. Tracey, J. Micromech. Microeng. **24**, 035017 (2014).
[43] W. Thielicke and E. J. Stamhuis, J. Open Res. Software **2**, e30 (2014).
[44] J. Barber, *Contact Mechanics*, Solid Mechanics and Its Applications Vol. 250 (Springer International Publishing, Cham, 2018).
[45] R. Zilionis, J. Nainys, A. Veres, V. Savova, D. Zemmour, A. M. Klein, and L. Mazutis, Nat. Protocols **12**, 44 (2016).